Bead parameterization of desktop and room-scale material extrusion additive manufacturing: How print speed and thermal properties affect heat transfer

*Tone D'Amico[1] and Amy M. Peterson[1,2]**

[1]Department of Chemical Engineering, Worcester Polytechnic Institute, 100 Institute Road, Worcester, MA 01609

[2]Department of Plastics Engineering, University of Massachusetts Lowell, 1 University Ave, Lowell, MA 01854

*Corresponding author: amy_peterson@uml.edu

Abstract

Material extrusion (MatEx) additive manufacturing ranges in size scale from the desktop scale fused filament fabrication (FFF) to the room scale big area additive manufacturing (BAAM). The principles of how FFF and BAAM operate are similar – polymer feedstocks are heated until molten and then extruded to form three-dimensional parts through layer-by-layer additive manufacturing. However, the scales of FFF and BAAM differ substantially, which leads to critical differences in thermal behavior for these thermally-driven processes. This study compares heat transfer in FFF and BAAM using finite element thermal modeling. Parameterization is performed across material properties, layer number, and print speed at the desktop and room scale for MatEx. BAAM stays hotter than FFF for a longer period of time, which facilitates interlayer diffusion and weld formation, but can also lead to slumping or sagging. Changes in thermal diffusivity affect FFF more than BAAM, with FFF exhibiting a local maximum in weld time at the thermal diffusivity of ABS. In all cases, weld time is longer than relaxation time, indicating that polymer reorientation and interdiffusion is possible. For BAAM, the temperature and thermal history of the center of an extruded bead differs greatly from the surface of the bead, which has important implications for process monitoring, property prediction, and part performance.

Keywords: material extrusion, fused filament fabrication, big area additive manufacturing, finite element analysis, heat transfer

1. Introduction

Material extrusion (MatEx) additive manufacturing, in which material is selectively dispensed through a nozzle to created printed structures, is the most common form of additive manufacturing (AM). Thermally-driven forms of MatEx range from the desktop scale fused filament fabrication (FFF), which was invented and patented as fused deposition modeling (FDM) by Stratasys co-founder Scott Crump [1], to the room scale big area additive manufacturing (BAAM). The principles of how FFF and BAAM operate are similar – polymer feedstocks are heated until molten and then extruded through a nozzle as the extruder rasters in the x and y planes to form a single layer, then the process is repeated on top of the newly printed layer until the final

part has been fabricated in a layer-by-layer fashion. However, as is highlighted in Table 1, the scales of FFF and BAAM differ substantially.

Table 1: Comparison of FFF and BAAM process parameters, highlighting the orders of magnitude differences in each.

	FFF	**BAAM**
Build Space (m^3)	$\sim 10^{-2}$	25
Extruder Nozzle Diameter (mm)	0.4	5-13
Layer Thickness (mm)	0.02-0.4	25-50
Deposition Rate (kg/hr)	0.07	36

FFF is widely used in prototyping, education, resource austere environments, and hobbyist applications [2–11]. While the cost and performance of FFF parts have historically not been competitive with traditionally manufactured parts for full production, FFF is incredibly useful for the design phase and drastically shortens the design cycle. Fundamental and applied research towards performance improvement and cost reduction of FFF are ongoing, and substantial progress has been made, in particular over the past five years [12–25].

BAAM was invented through a collaboration between Oak Ridge National Laboratory's Manufacturing Demonstration Facility (MDF) and Cincinnati in 2014 [26]. Since then, BAAM has found application in rapid prototyping at scale, such as for automotive design, and also in tooling [15,27]. Tooling is well-suited to AM, since it requires single-to-short runs and is a field where lead times for traditional parts range from many weeks to many months. Furthermore, the design complexity that AM offers provides additional advantages as compared to traditional manufacturing [28].

FFF and BAAM both use polymer feedstocks. In FFF, material is provided in the form of filament. Filament diameter and its consistency are very important to print quality and mechanical properties. While most desktop scale thermally-driven printers are filament-fed, a few printers are pellet-fed [29–31]. BAAM uses polymer pellets as a feedstock, which facilitates higher deposition rates. Polymer pellets are also ~2 orders of magnitude less expensive than comparable filaments.

The first BAAM prints were performed with acrylonitrile butadiene styrene (ABS), a very common material for FFF; however, these prints warped substantially, so subsequent prints were performed with a chopped carbon fiber-ABS composite [19,32–34]. Other materials that have been printed on the BAAM scale include glass fiber-reinforced ABS, poly(lactic acid) (PLA), wood fiber-reinforced PLA, polyethylene terephthalate glycol-modified (PETG), carbon fiber-reinforced polyphenylene sulfide (PPS), carbon fiber-reinforced polyphenylsulfone (PPSU), polypropylene (PP), and a sand-PP composite [35–39].

Despite the similarities between FFF and BAAM, the substantial differences in scale affect heat transfer, which plays an important role in inter- and intralayer welding, warping, slumping/sagging, and dimensional integrity. A recent review of thermal modeling of MatEx processes found that, in general, modeling approaches recommend higher extruder and bed temperatures for improved weld strength, although residual thermal stresses had also been found to increase with higher extruder temperatures [40]. Choo et al. found, via experiments and modeling of BAAM, that slower cooling through additional thermal mass led to slumping of large scale MatEx structures [35]. Compton et al. identified layer time, the amount of time between printing one layer at a given x-y location and the next layer at the same x-y location, as an important consideration for BAAM: If the layer time is low, the layer onto which printing is occurring will remain above the polymer's glass transition temperature (T_g), which facilitates interlayer diffusion. However, if the layer time is too long, the lower layer will cool too much, leading to less welding and a propensity for delamination [34].

This study compares heat transfer in FFF and BAAM through finite element thermal modeling. Parameterization is performed across material properties, layer number, and print speed at the desktop and room scale for MatEx.

2. Materials and Methods

2.1 Finite Element Analysis Model

A finite element analysis-based simulation was built in COMSOL Multiphysics that accounts for convective heat transfer with surroundings, conductive heat transfer with the heated build plate and nozzle, and heat transfer due to material deposition. Additionally, radiative heat

transfer with surroundings is accounted for in BAAM models unless otherwise noted. Radiation is neglected at the FFF scale because its effect on heat transfer was previously found to be negligible [41].

Internal heat transfer was calculated using:

$$\rho\widehat{C_p}\frac{dT}{dt} + \nabla \cdot \vec{q} = 0 \qquad (1)$$

where ρ is density, $\widehat{C_p}$ is the specific heat capacity, T is temperature, t is time, and $\vec{q}$ is the heat flux vector.

External heat transfer comprises conduction, convection, radiation, and addition of hot material. Both the nozzle, at $T_n = 230°C$, and build plate, at $T_p = 110°C$ for BAAM scale models and $T_p = 115°C$ for FFF scale models, transfer heat via conduction. Model temperatures were chosen based on typical experimental conditions and conversations with Mr. Sam Pratt of NSWCCD [24,35,36,41,42]. Conduction from the build plate was accounted for by setting the temperature of the surface in contact with the print bed (bottom surface) to T_p. To account for conduction between the nozzle and the print surface, thermal resistivity of the interface between the nozzle and part was switched between very high ($1 \times 10^{7}\ \frac{K \cdot m^2}{W}$) and very low ($1 \times 10^{-11}\ \frac{K \cdot m^2}{W}$) values depending on if the nozzle was in contact with the surface (low) or not (high).

Convective heat transfer with surrounding air was implemented as a convective heat transfer heat flux boundary condition in COMSOL. For this work, it was assumed only natural convection took place. The boundary condition was given by:

$$q = h * (T - T_a) \qquad (2)$$

where h is the heat transfer coefficient, which was calculated based on the surrounding material (air), ambient temperature (T_a), and pressure (p, 1 atm). Ambient air temperature was assumed to be $T_a = 25°C$ for FFF and $T_a = 43°C$ for BAAM and remain constant throughout the simulation. For FFF, this boundary condition was selected due to the details of the experimental setup of Seppala and Migler, in which the front of the printer was required to stay open to allow for IR thermography of the print [43]. For BAAM, this value is consistent with the experimental environment.

Radiation was previously shown to be negligible in FFF [41]. However, the thermal mass associated with BAAM is substantially larger, so radiation cannot be neglected *a priori*. Indeed, prior models of heat transfer in BAAM have included radiation as a heat transfer mechanism [34,35]. Therefore, radiation was neglected for FFF models, but is included in BAAM models unless otherwise noted. Radiation is calculated by:

$$q_{rad} = \varepsilon\sigma(T^4 - T_a^4) \quad (3)$$

where ε is the emissivity and has a value of 0.87 [34,35] and σ is the Stefan-Boltzmann constant. As is discussed in the Results and Discussion, radiative heat transfer is greatest on the surface immediately following the nozzle. The default BAAM model presented in this work accounts for radiation only on the top surface of the print.

Further simulation details are available in previous work [41].

2.2 Material Properties

ABS material properties are used for all simulations and relative thermal diffusivities are given with respect to the thermal diffusivity of ABS. C360 brass is used as the nozzle material, which is consistent with experiments. For this work, material properties of ABS at 25°C and brass at 20°C are used and are assumed to be constant throughout the simulation [44,45]. This reduces the complexity of the model, reducing solution time. Over the range of temperatures of interest in these simulations (25 – 230 °C), ABS density is reported to decrease by approximately 80 kg/m^3, which represents a 7-8% change [46], while heat capacity (C_p) increases by approximately 0.8 J/g·°C (20%), with the major increase occurring at T_g [47]. Since some material properties increase with increasing temperature, while other decrease, and the rates of these change are non-linear, the effect of assuming constant values cannot be simply asserted for an arbitrary temperature.

2.3 Model Geometry

The FFF geometry used in this work is based on the geometry used by Seppala and Migler, which is a 160 mm (x-axis) by 0.45 mm (y-axis) part consisting of single roads of thickness (z-axis) 0.3 mm [43]. For the current work, an x-dimension of 120 mm is used to reduce the volume

being simulated. This reduction in length does not affect temperature at the midpoint (x-axis) of the part [41]. The BAAM geometry is also a wall of single roads, but with dimensions of 914.4 mm (x-axis) by 9.636 mm (y-axis) and a 3.81 mm layer thickness.

In both geometries, the part has an x-y plane of symmetry and the nozzle does not move in the y-axis, so a symmetry boundary is used to further reduce the volume being simulated. The nozzle inner diameters for FFF and BAAM are 0.4 mm and 7.62 mm, respectively. Unless otherwise noted, the default print speed is 30 mm/s.

Thermal spectra are reported from the center of the x-axis of the print. For FFF, spectra are reported for the centerline (point of symmetry) of a weld, and for BAAM, spectra are provided at both the centerline and surface of a weld. For a given layer x, the thermal spectrum shown is at the interface of layers x and $x-1$ as layer x is being printed.

2.4 Time-temperature superposition and relaxation time

Interlayer diffusion and polymer welding are functions of time and temperature. Since MatEx is highly non-isothermal, the principle of time-temperature superposition (TTS) can be used to condense all time-temperature information to a single isothermal weld time. TTS states that phenomena occurring over long time periods at low temperatures are equivalent to phenomena occurring over short time periods at elevated temperatures. For amorphous polymers, this relationship can be described using the Williams-Landel-Ferry (WLF) equation:

$$\log a_T = \frac{-C_1(T-T_r)}{C_2+(T-T_r)} \qquad (4)$$

where C_1 and C_2 are material-specific constants determined by fitting to a master curve, a_T is the shift factor, and T_r is the reference temperature [48]. This approach has been used to calculate equivalent isothermal weld times for FFF [41,42,49].

Temperature vs. time data were converted to equivalent weld times ($t_{w,ref}$) at a reference temperature (T_{ref}) using:

$$t_{w,ref} = \int_0^{t_{final}} a_t^{-1} dt \qquad (5)$$

t_{final} is the end time for the data being converted. We chose T_{ref} to be T_g, which results in very large values of $t_{w,ref}$. A T_g value for ABS of 105°C was used.

3. Results and Discussion

3.1 Size Scale Comparison

Even though the principles of FFF and BAAM are the same, thermal profiles for differ greatly (Figure 1). FFF exhibits a relatively shorter heated tail behind the nozzle and heating into lower layers than BAAM, although BAAM facilitates heat transfer more effectively across larger distances. These results are consistent with thermography of FFF and BAAM [24,34,35,43]. Additionally, more uniform temperature is observed across the width of the road in FFF, which would lead to a more uniform bond.

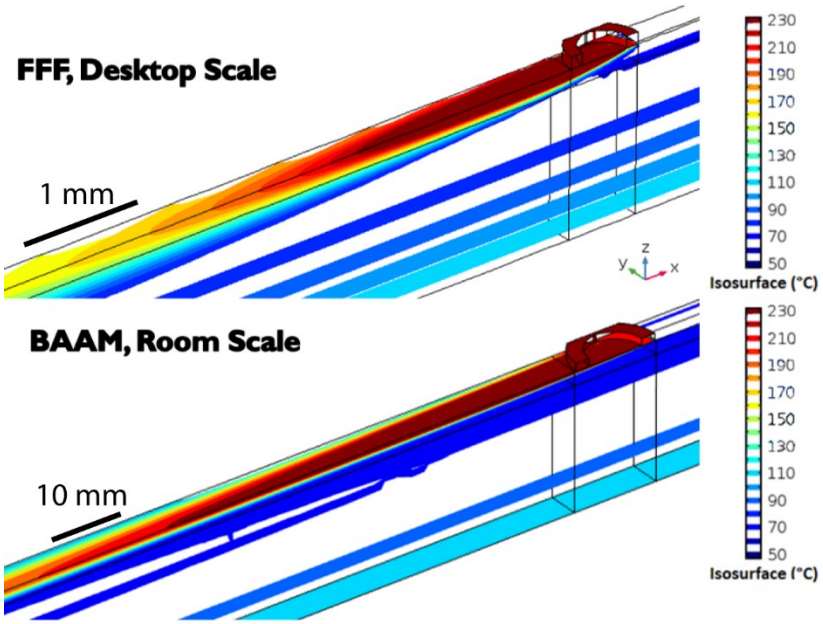

Figure 1: FFF and BAAM thermal profiles. Isosurface temperature are presented for both types of MatEx for an extruder temperature of 230°C, print speed of 30 mm/s, and material properties of ABS. Images are not to scale, scale bars represent x-axis scale only.

Radiative heat transfer at the FFF scale has been shown to have minimal effect on thermal profiles [41], while simulations demonstrate a noticeable effect of radiation at the BAAM scale (Figure 2). Without radiative heat transfer, the heated tail is longer, which increases predicted weld time – this is because conduction through the part becomes a more significant heat transfer mechanism when radiation from a surface is not allowed. Additionally, radiative heat transfer is concentrated directly behind the nozzle, with surface radiosity highest in a small area trailing the nozzle (Figure 3). Therefore, radiative heat transfer calculations do not need to be run for the entire

surface in order to capture radiative effects. Since these calculations are computationally expensive, running radiative heat transfer calculations on only the top surface decreases computation workload substantially and was the approach taken in this work.

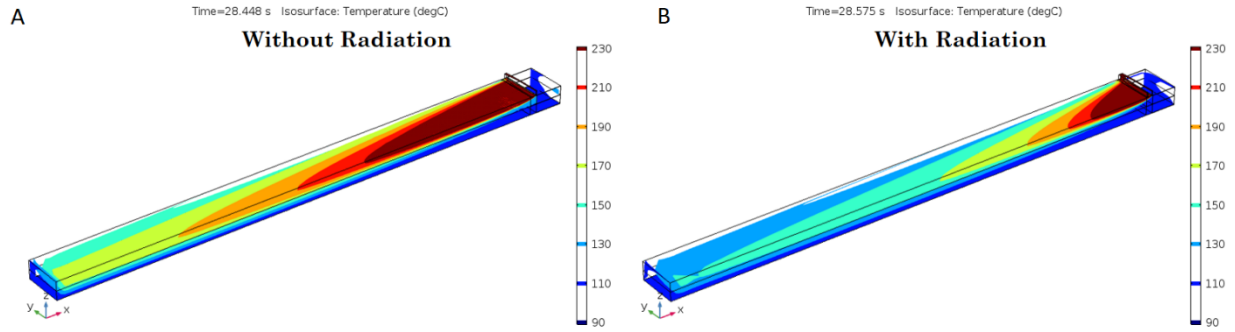

Figure 2: BAAM isosurfaces A) with and B) without radiation. Note that the y dimension is extended relative to the x direction in order to improve clarity (y dimension of printed structure is 4.818 mm, while the x dimension is 914.4 mm).

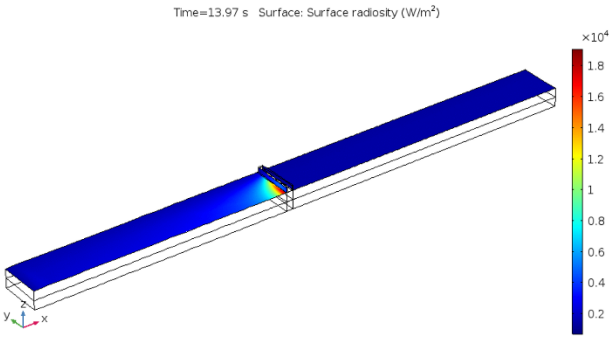

Figure 3: Surface radiosity of a BAAM structure during printing. BAAM radiative heat transfer is concentrated just behind nozzle.

Temperatures of recently deposited ABS in FFF drop below T_g within one to three seconds, indicating a limited window for polymer interdiffusion and reorientation [24,43]. Our model is able to replicate these time scales in FFF [41]. At the BAAM scale, cooling to T_g takes much longer: an ABS triangle with a 4-bead thick wall cooled below T_g in approximately seven minutes and required approximately 30 minutes to cool to 60°C [26]. These long time scales are reflected in our model (Figure 4). As with FFF, temperature spectra have similar shapes across all layers. Depositing a new layer increases the previous layers temperature after a several second lag period, an artifact of this modeling approach to MatEx in which material deposition was modeled as a uniform increase in z dimension across the entire build plane, with heat transfer due to material

deposition implemented at the top surface. This lag, which is not observed in FFF simulations, results from the larger distance (3.81 mm vs. 0.3 mm) through which heat must conduct in order to reach the weld surface.

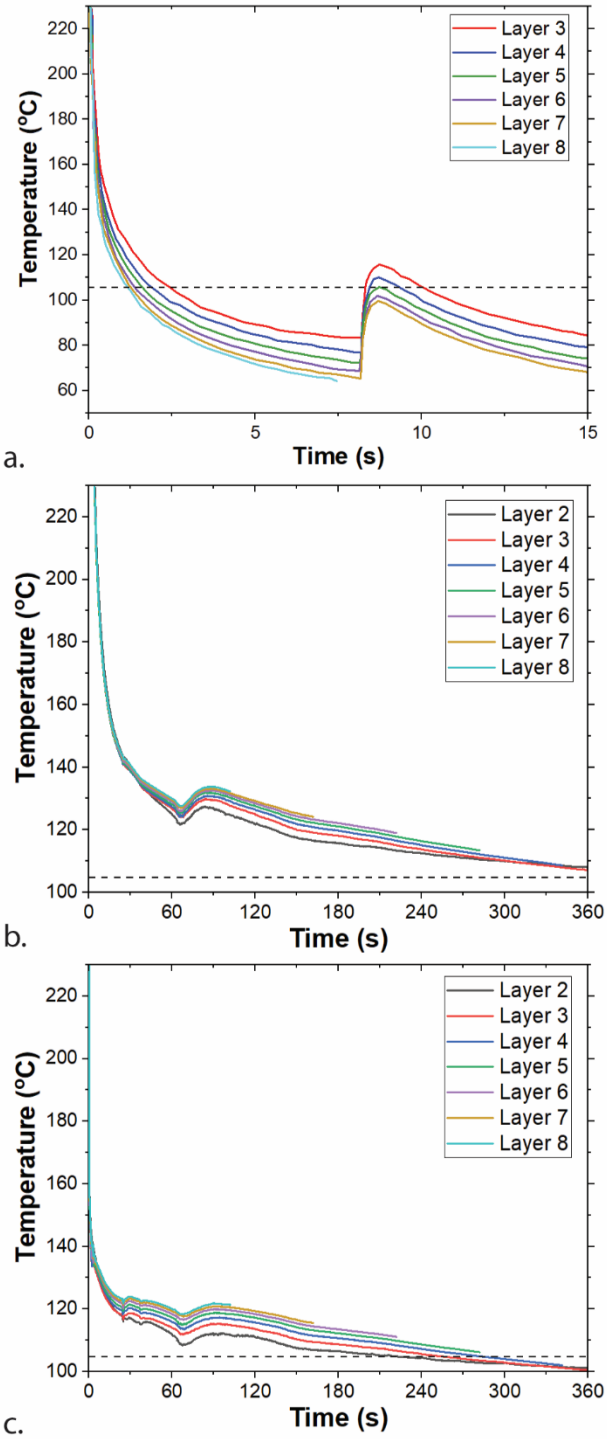

Figure 4: Thermal spectra in A) FFF, B) BAAM along the centerline, and C) along the outside of the part.

The temperature spike when a new layer is added is smaller for BAAM than FFF. A smaller thermal spike is also consistent with the increased conduction distance, since heat can spread more in the x- and y-axes with a larger thickness. Internal and external temperature profiles both remain above T_g over the observed period; however, external temperatures drop more rapidly after deposition and have a more delayed and smaller temperature spike than internal temperatures. The difference in these temperature profiles highlight the non-uniformity of temperature along the width of a BAAM road.

3.2 Role of Thermal Diffusivity

Thermal diffusivity, a measure of the rate of heat transfer of a material, is described by:

$$\alpha = \frac{k}{\rho C_p} \qquad (6)$$

where k is thermal conductivity. In exploring the role of material properties on heat transfer in MatEx, we chose to vary thermal diffusivity. Thermal diffusivity was normalized to that of ABS, such that a relative thermal diffusivity (a_{rel}) of 1 corresponds to α of ABS. Addition of carbon fiber to ABS increases thermal conductivity more than density and heat capacity, so chopped carbon fiber in ABS, which is a common BAAM material [26,27,50], would be expected to have a higher thermal diffusivity than ABS ($a_{rel} > 1$).

In modeling of FFF, the temperature of a given point is observed to decrease over time until it reaches its minimum temperature (T_{min}), which is also a steady state temperature for that point during printing (Figure 5). Figure 5A shows times to minimum/steady state temperature for three relative thermal diffusivities and Layers 3-8. For the ABS condition, T_{min} is achieved in 10-50 seconds. T_{min} and time to T_{min} decrease with increasing layer number up to Layer 7. This trend is likely due to earlier layers being closer to the heated build plate and, therefore, having a higher steady state temperature. For a_{rel} = 0.5, all T_{min} are achieved in approximately 10 seconds, although these temperatures have a 15 °C range. As shown in Figure 5C, Layers 3 and 4 have higher steady state temperatures, and subsequent layers all exhibit a steady state of ~ 55 °C. For a_{rel} = 2, time to T_{min} is longer for lower layers (60 vs. 40 seconds for Layer 3) and eventually reaches the same ~ 10 second time to T_{min} for Layer 8. For a given layer, T_{min} increases with

increasing a_{rel} because higher thermal diffusivities allow the build plate to affect temperatures further into the part.

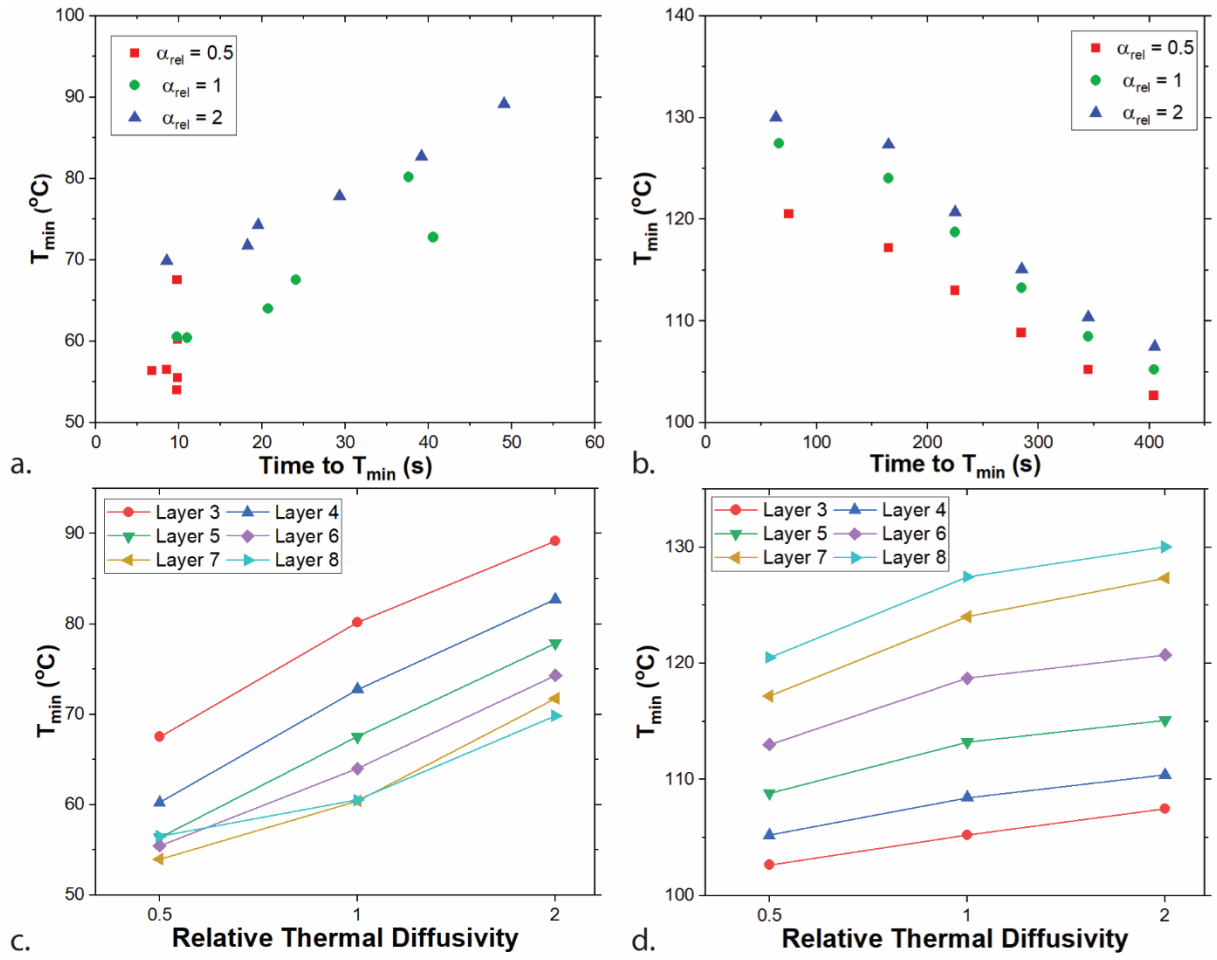

Figure 5: Minimum temperature vs. time for A) FFF at 50 mm/s and B) BAAM at 30 mm/s. Minimum temperature vs. relative thermal diffusivity in C) FFF at 50 mm/s and D) BAAM at 30 mm/s.

In BAAM, T_{min} decreases with increasing simulation time (i.e. number of additional layers printed) for most layers – when this is the case, T_{min} does not represent a steady state temperature. Since the steady state temperatures are not reached for most layers, we see an opposite trend in T_{min} vs. time to T_{min} for BAAM (Figure 5B) as compared to FFF (Figure 5A). The shortest times are for the highest layer (Layer 8), with both time and T_{min} decreasing with decreasing layer number (Figure 5D). Longer cooling times in BAAM are necessitated by its lower surface area:volume, limiting the rate at which energy can be convected and radiated away from the part. T_{min} increases with increasing a_{rel} for BAAM; however, most T_{min} do not represent steady state temperatures. These modeling results are consistent with Compton et al.'s experimental findings,

wherein the first layer of a 20% chopped carbon fiber-ABS wall cooled to 100°C in approximately 500 seconds, while layer 15 required over double that amount of time to cool to 100°C [34]. It should be noted, however, that T_{min} in these experiments ranged from 50°C for layer 1 to 22°C for layer 30, which is due in part to their lower bed and ambient temperatures.

For FFF, T_{min} decreases moving away from the heated build plate and begin to converge by layers seven and eight. BAAM, by contrast, shows increasing T_{min} moving away from the heated build plate. This is due to later layers not having sufficient time to cool. Another point of difference between FFF and BAAM is the time scale necessary to reach a steady state temperature – for FFF, layers cool within one minute, while BAAM requires over six minutes. Additionally, the steady state temperatures for FFF are much lower than those for BAAM.

As temperatures below T_g do not allow for substantial polymer chain mobility over reasonable time scales, the time spent above T_g is of interest. Increased cooling time in BAAM meant the entire printed structure, except for Layers 3 and below for a_{rel} = 0.5, remained above T_g over the time period simulated. Given the impact of the heated build plate on lower layers, it is expected that higher layers have lower steady state temperatures, meaning Layers 4 and above cool below T_g during printing.

In contrast, FFF exhibits a drop below T_g within just a few seconds, limiting time for both relaxation and weld formation (Figure 6). Varying a_{rel} highlights two underlying, competing forces. Near the heated build plate, conduction with the build plate dominates. Increasing thermal diffusivity causes more conduction from the build plate, which increases time to T_g. Far from the build plate, conduction to the part surface where heat can be convected away is more important. Increasing thermal diffusivity increases conduction to the surface, so decreases time to T_g. Between these extremes, competition between these two can be seen in the time to T_g for several layers. Though the single wall geometry used here is an extreme example in terms of surface area:volume, these results do suggest that, for many geometries, increasing thermal diffusivity will cause FFF parts to cool more rapidly.

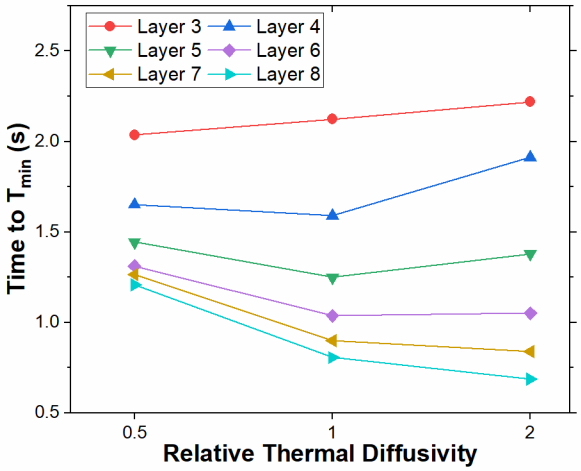

Figure 6: Response of time to T_g to changes in thermal diffusivity in FFF at 50 mm/s.

Time-temperature superposition can be applied through the WLF equation (Equation 4) to collapse the temperature data for a point over the course of a build to a single time at a reference temperature [24,41,42,48,49]. This isothermal equivalent weld time (t_w) has been shown to predict tear energy consistent with polymer weld theory [42,51–53]. FFF shows maximum t_w for a_{rel} = 1, with lower weld time when a_{rel} is either increased or decreased (Figure 7A). ABS is widely used in FFF [19], and this suggests its thermal properties and density may be specifically well-suited to the process.

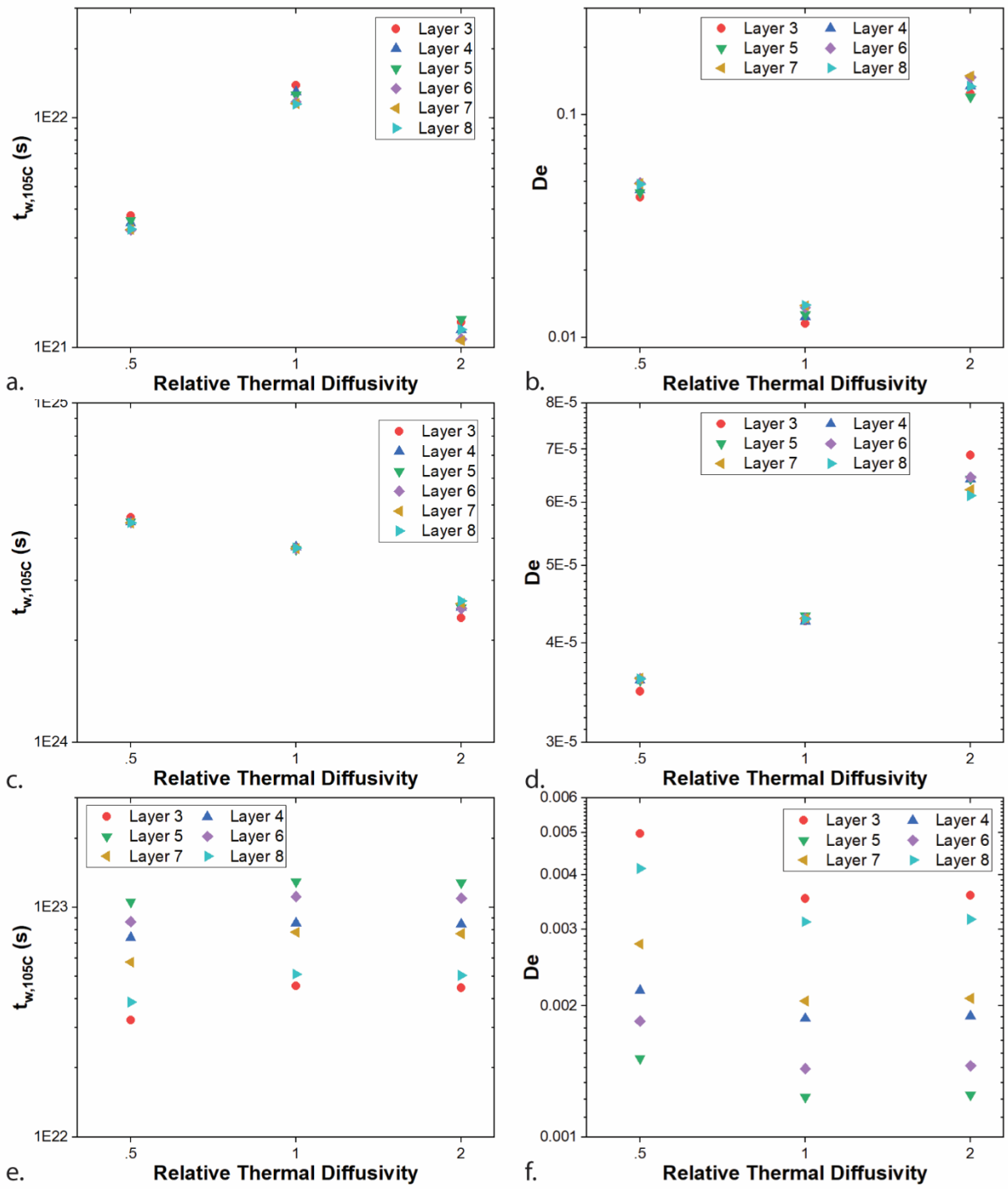

Figure 7: Isothermal equivalent weld times A) for FFF at 50 mm/s, C) internally for BAAM at 30 mm/s, and E) externally for BAAM at 30 mm/s. Deborah numbers B) for FFF, D) internally for BAAM, and F) externally for BAAM.

Longer weld times will lead to interfaces that more resemble the bulk and are, therefore, stronger. However, when weld times are longer than the time necessary to reach equilibrium

interdiffusion ($t_w > t_\infty$), additional weld time does not provide a benefit [54]. In fact, additional weld time in this case can lead to slumping of the entire printed structure [55]. In order to explore weld times in a bit more detail, the Deborah number was calculated for each layer. The Deborah number describes the relationship between relaxation time of a viscoelastic material (λ) and the characteristic time of a process. For the case of MatEx,

$$De = \frac{\lambda}{t_w} \qquad (7)$$

When De = 0, a material behaves as a viscous fluid and the printed structure will be prone to slumping. When $De = \infty$, a material behaves as an elastic solid and no welding occurs. ABS describes a wide range of formulations of complex engineered plastics with multiple relaxation times, so for this analysis, only the longest relaxation time is considered. Aoki et al. found the longest relaxation time varied with formulation, with the highest observed λ for ABS on the order of 10^2 seconds at 200°C [56]. For FFF, De shows a minimum at a_{rel} = 1 (Figure 1B). All values fall within a small range (0.01 – 0.15), with the highest De at a_{rel} = 2.

BAAM exhibits weld times orders of magnitude higher than those in FFF and does not have a maximum weld time at a_{rel} = 1 (Figure 7C). Instead, weld time decreases with increasing thermal diffusivity. Given much higher weld times, De values in BAAM are all much smaller than those in FFF (Figures 7D and 7F). For the center of the bead, De values range from $3 \times 10^{-5} - 7 \times 10^{-5}$, while external values range from $1.2 \times 10^{-3} - 5 \times 10^{-3}$. Internal De values increase with increasing a_{rel}; however, external values are somewhat higher for a_{rel} = 0.5. While sufficient energy to achieve welding is not a concern at these low values of De, slumping can occur.

External locations in BAAM exhibit lower weld times than internal ones, which is consistent with them being exposed to air and immediately convecting away heat. They also show a smaller, but positive thermal diffusivity response. This can be attributed to their location; increased thermal diffusivity decreases weld time in other cases because heat is more rapidly conducted to the edges and then convected away. For external points, heat is already at the surface, so this effect is not relevant and increasing thermal diffusivity only increases the impact of the heated build plate, increasing weld time. The large differences in behavior between internal and surface points in BAAM are a concern for residual thermal stress formation. Indeed, residual stresses and the warping and delamination they cause are important design challenges for BAAM [34,55,57].

3.3 Effect of Print Speed

In previous work, we observed that T_{min} increased with increasing print speed for FFF [41]. For BAAM, this increase in T_{min} is much larger (Figure 8), with a 110 °C increase in T_{min} as print speed increased from 10 mm/s to 100 mm/s. In comparison, T_{min} increased approximately 10 °C over the same print speed range in FFF. As discussed previously, we attribute some of this difference to the relationship between T_{min} and the time to reach T_{min}. At 10 mm/s, the relation is flat, suggesting a steady state has been reached. However, 30 mm/s and 100 mm/s results suggest that cooling is still taking place. With higher print speeds, layer times and the time being simulated are shorter: the layer times for 10 mm/s, 30 mm/s, and 100 mm/s prints are 183 s, 61 s, and 18 s, respectively. Using the layer time approach from Compton et al., at a print speed of 10 mm/s, the top layer cools below the critical temperature of 110 °C and would be susceptible to warping, which is consistent with its long layer time [34].

For 30 mm/s and 100 mm/s, the highest T_{min} is observed for layer 8, and layer temperature decrease with decreasing layer number. These results provide further evidence that cooling is still taking place at the end of the simulation of 30 mm/s and 100 mm/s print speeds. At 10 mm/s, the highest temperature layer is layer 3 at 84.6 °C; however, all values of T_{min} for 10 mm/s are within a 6.1 °C range. Layer 3 may exhibit the highest T_{min} value at 10 mm/s because of its relative proximity to the heated print bed.

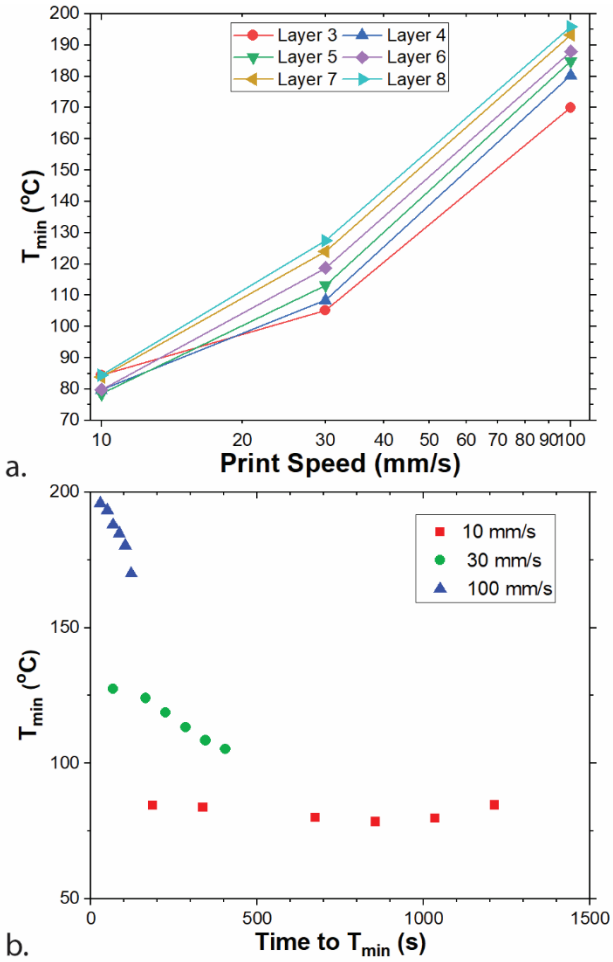

Figure 8: A) Effect of print speed in BAAM on minimum temperature. B) Relationship between time to minimum temperature and layer minimum temperature for three print speeds in BAAM.

Experimental and simulation work at the FFF scale has shown print speed has little impact on weld times and resultant weld strength [41,42,49]. Increasing print speed increases the rate at which heat is added to the part due to material deposition, but heat is still only removed by convection and radiation from the part surface. In FFF, very low print speeds cools more slowly because the heated nozzle stays in contact longer. However, this effect was not seen in BAAM simulations (Figure 9). Internally, weld time increases with increasing print speed, consistent with increased heat flow in due to material deposition. Externally, changes in weld time are smaller and tend towards decreasing with increasing print speed. This may be due to the speed at which the heat nozzle moves away, similar to FFF. For both internal and external points, De is near zero, indicating complete welds could be formed for all tested print speeds. Internal Deborah numbers

at a print speed of 100 mm/s are all less than 10^{-60}, meaning enough energy is added to the system for the polymer to behave as a viscous fluid, i.e. slumping is a major concern at this layer time.

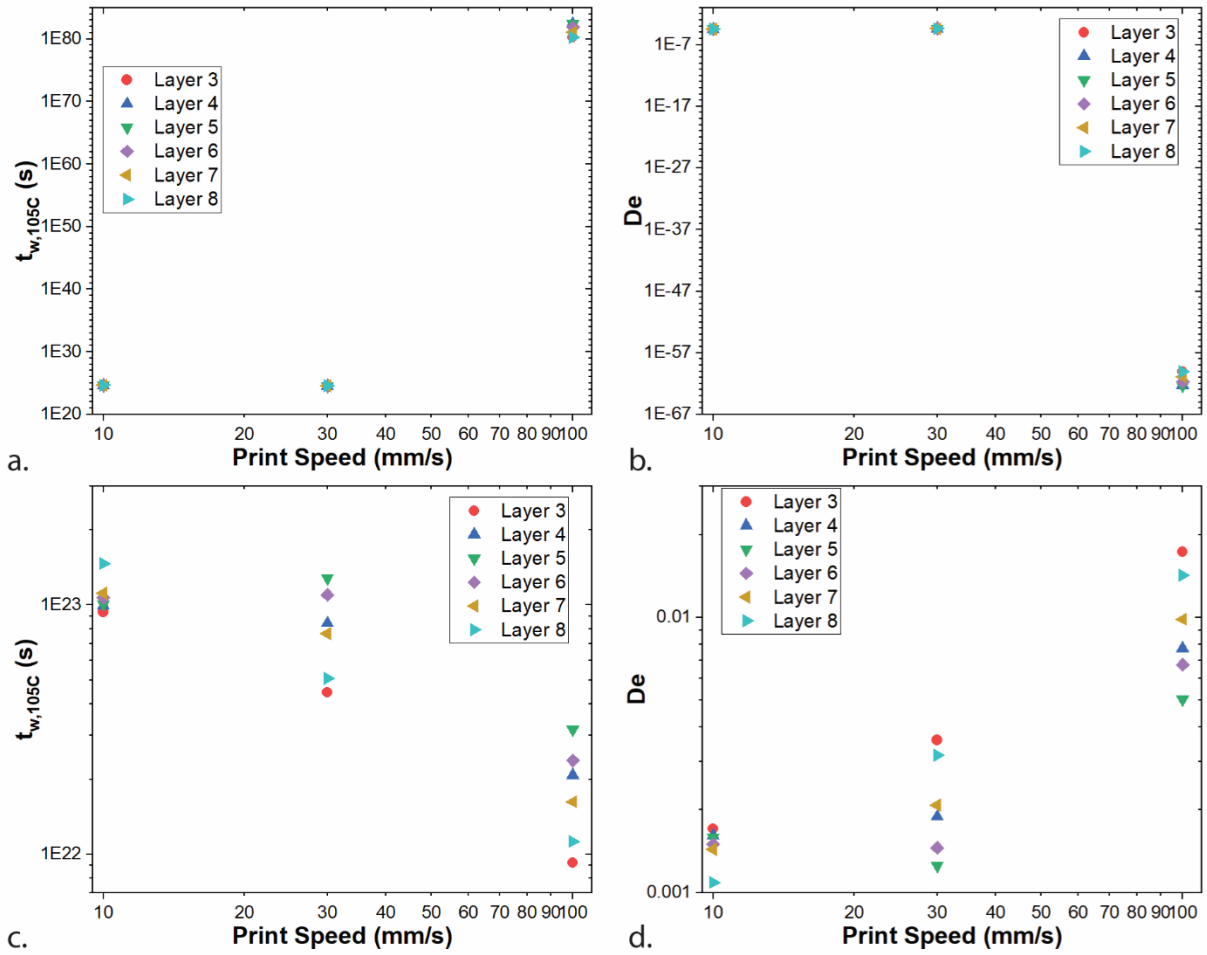

Figure 9: Weld time for BAAM increases at 100 mm/s for A) internal points, but B) De is still very small for all print speeds due to the high weld time. For B) external points, weld time decreases with print speed but D) De remains between 0.001 and 0.02.

3. Conclusion

FFF and BAAM are both MatEx processes that transform a polymer feedstock into three-dimensional parts through layer-by-layer AM. However, the difference in size scale leads to critical differences in thermal behavior for these thermally-driven processes. BAAM stays hotter than FFF for a longer period of time. This facilitates interlayer diffusion and weld formation, but can also lead to slumping or sagging. Due to the large thermal mass of BAAM structures, radiation is a significant form of heat transfer in BAAM, but not in FFF. Additionally, FFF layers reached

steady-state temperatures during printing, while only the slowest print speed for BAAM resulted in layers reaching steady-state temperatures during printing.

Changes in thermal diffusivity affect FFF more than BAAM. FFF exhibits a local maximum in weld time at the thermal diffusivity of ABS, while BAAM weld time decreases slightly with increasing thermal diffusivity. In all cases, weld time is longer than relaxation time, indicating that polymer reorganization and interdiffusion is possible. For BAAM, the temperature and thermal history of the center of an extruded bead differs greatly from the surface of the bead, which is an important considering if thermography will be used for process control or property prediction.

Acknowledgements

The authors thank Lonnie Love, Vlastimil Kunc, Sam Pratt, and Jennifer Wolk for insightful discussions and guidance, especially in understanding BAAM. The authors also acknowledge the Academic and Research Computing team at WPI, especially Siamak Najafi and Ermal Toto.

Funding

This work was supported by the Office of Naval Research (N00014-17-1-2672) and National Science Foundation (DGE-1144804 and CMMI-1853480).

References

[1] S.S. Crump, Apparatus and method for creating three-dimensional objects, 5,121,329, 1989.

[2] A. Kiełbus, K. Furyk-Grabowska, K. Ostrowska, Application of FFF Method in Orthopedics, Mach. Dyn. Res. 40 (2016) 67–78.

[3] G.D. Goh, V. Dikshit, A.P. Nagalingam, G.L. Goh, S. Agarwala, S.L. Sing, J. Wei, W.Y. Yeong, Characterization of mechanical properties and fracture mode of additively manufactured carbon fiber and glass fiber reinforced thermoplastics, Mater. Des. 137 (2018) 79–89. doi:10.1016/j.matdes.2017.10.021.

[4] J. Go, A.J. Hart, Fast Desktop-Scale Extrusion Additive Manufacturing, Addit. Manuf. 18 (2017) 276–284. doi:10.1016/j.addma.2017.10.016.

[5] D.S. Kaliakin, R.R. Zaari, S.A. Varganov, 3D Printed Potential and Free Energy Surfaces for Teaching Fundamental Concepts in Physical Chemistry, J. Chem. Educ. 92 (2015) 2106–2112. doi:10.1021/acs.jchemed.5b00409.

[6] P.P. Rodenbough, W.B. Vanti, S.-W. Chan, 3D-Printing Crystallographic Unit Cells for Learning Materials Science and Engineering, J. Chem. Educ. 92 (2015) 1960–1962. doi:10.1021/acs.jchemed.5b00597.

[7] S.C. Meyer, 3D Printing of Protein Models in an Undergraduate Laboratory: Leucine Zippers, J. Chem. Educ. 92 (2015) 2120–2125. doi:10.1021/acs.jchemed.5b00207.

[8] K.R. Hart, J.B. Frketic, J.R. Brown, Recycling meal-ready-to-eat (MRE) pouches into polymer fi lament for material extrusion additive manufacturing, Addit. Manuf. 21 (2018) 536–543. doi:10.1016/j.addma.2018.04.011.

[9] N.E. Zander, M. Gillan, R.H. Lambeth, Recycled polyethylene terephthalate as a new FFF feedstock material, Addit. Manuf. 21 (2018) 174–182. doi:10.1016/j.addma.2018.03.007.

[10] N.E. Zander, M. Gillan, Z. Burckhard, F. Gardea, Recycled polypropylene blends as novel 3D printing materials, Addit. Manuf. 25 (2019) 122–130. doi:10.1016/j.addma.2018.11.009.

[11] B. Wittbrodt, J.M. Pearce, The effects of PLA color on material properties of 3-D printed components, Addit. Manuf. 8 (2015) 110–116. doi:10.1016/j.addma.2015.09.006.

[12] G.W. Melenka, J.S. Schofield, M.R. Dawson, J.P. Carey, Evaluation of dimensional accuracy and material properties of the MakerBot 3D desktop printer, Rapid Prototyp. J. 21 (2015) 618–627. doi:10.1108/RPJ-09-2013-0093.

[13] G.W. Melenka, B.K.O. Cheung, J.S. Schofield, M.R. Dawson, J.P. Carey, Evaluation and prediction of the tensile properties of continuous fiber-reinforced 3D printed structures, Compos. Struct. 153 (2016) 866–875. doi:10.1016/j.compstruct.2016.07.018.

[14] F. Peng, Z. Zhao, X. Xia, M. Cakmak, B.D. Vogt, Enhanced Impact Resistance of Three-

Dimensional-Printed Parts with Structured Filaments, ACS Appl. Mater. Interfaces. 10 (2018) 16087–16094. doi:10.1021/acsami.8b00866.

[15] B. Brenken, E. Barocio, A. Favaloro, V. Kunc, R.B. Pipes, Fused filament fabrication of fiber-reinforced polymers: A review, Addit. Manuf. 21 (2018) 1–16. doi:10.1016/j.addma.2018.01.002.

[16] M. Spoerk, F. Arbeiter, H. Cajner, J. Sapkota, C. Holzer, Parametric optimization of intra- and inter-layer strengths in parts produced by extrusion-based additive manufacturing of poly(lactic acid), J. Appl. Polym. Sci. 134 (2017) 45401. doi:10.1002/app.45401.

[17] J. Bartolai, T.W. Simpson, R. Xie, Predicting strength of additively manufactured thermoplastic polymer parts produced using material extrusion, Rapid Prototyp. J. 24 (2018) 321–332. doi:10.1108/RPJ-02-2017-0026.

[18] R.M. Dunn, K.R. Hart, E.D. Wetzel, Improving fracture strength of fused filament fabrication parts via thermal annealing in a printed support shell, Prog. Addit. Manuf. 4 (2019) 233–243. doi:10.1007/s40964-019-00081-x.

[19] A.M. Peterson, Review of acrylonitrile butadiene styrene in fused filament fabrication: a plastics engineering-focused perspective, Addit. Manuf. 27 (2019) 363–371. doi:10.1016/j.addma.2019.03.030.

[20] D.J. Braconnier, R.E. Jensen, A.M. Peterson, Processing parameter correlations in material extrusion additive manufacturing, Addit. Manuf. 31 (2020) 100924. doi:10.1016/j.addma.2019.100924.

[21] C. Luo, X. Wang, K.B. Migler, J.E. Seppala, Upper bound of feed rates in thermoplastic material extrusion additive manufacturing, Addit. Manuf. 32 (2020) 101019. doi:10.1016/j.addma.2019.101019.

[22] O. Holzmond, X. Li, In situ real time defect detection of 3D printed parts, Addit. Manuf. 17 (2017) 135–142. doi:10.1016/j.addma.2017.08.003.

[23] J. Go, S.N. Schiffres, A.G. Stevens, A.J. Hart, Rate limits of additive manufacturing by fused filament fabrication and guidelines for high-throughput system design, Addit. Manuf. 16 (2017) 1–11. doi:10.1016/j.addma.2017.03.007.

[24] J.E. Seppala, S.H. Han, K.E. Hillgartner, C.S. Davis, K.B. Migler, Weld formation during material extrusion additive manufacturing, Soft Matter. 13 (2017) 6761–6769. doi:10.1039/c7sm00950j.

[25] P. Minetola, M. Galati, A challenge for enhancing the dimensional accuracy of a low-cost 3D printer by means of self-replicated parts, Addit. Manuf. 22 (2018) 256–264. doi:10.1016/j.addma.2018.05.028.

[26] R.B. Dinwiddie, V. Kunc, J.M. Lindal, B. Post, R.J. Smith, L. Love, C.E. Duty, Infrared imaging of the polymer 3D-printing process, in: Proc. SPIE, 2014: p. 910502. doi:10.1117/12.2053425.

[27] C. Ajinjeru, V. Kishore, J. Lindahl, Z. Sudbury, A.A. Hassen, B. Post, L. Love, V. Kunc, C. Duty, The influence of dynamic rheological properties on carbon fiber-reinforced polyetherimide for large-scale extrusion-based additive manufacturing, Int. J. Adv. Manuf. Technol. 99 (2018) 411–418. doi:10.1007/s00170-018-2510-z.

[28] M. Chapiro, Current achievements and future outlook for composites in 3D printing, Reinf. Plast. 60 (2016) 372–375. doi:10.1016/j.repl.2016.10.002.

[29] N. Kumar, P.K. Jain, P. Tandon, P.M. Pandey, Investigation on the effects of process parameters in CNC assisted pellet based fused layer modeling process, J. Manuf. Process. 35 (2018) 428–436. doi:10.1016/j.jmapro.2018.08.029.

[30] Wohlers Associates, Wohlers Report 2018 3D Printing and Additive Manufacturing State of the Industry Annual Worldwide Progress Report, Fort Collins, CO, 2018.

[31] J.J. Fallon, S.H. McKnight, M.J. Bortner, Highly loaded fiber filled polymers for material extrusion: A review of current understanding, Addit. Manuf. 30 (2019) 100810. doi:10.1016/j.addma.2019.100810.

[32] L.J. Love, V. Kunc, O. Rios, C.E. Duty, A.M. Elliott, B.K. Post, R.J. Smith, C.A. Blue, The importance of carbon fiber to polymer additive manufacturing, J. Mater. Res. 29 (2014) 1893–1898. doi:10.1557/jmr.2014.212.

[33] V. Kishore, C. Ajinjeru, A. Nycz, B. Post, J. Lindahl, V. Kunc, C. Duty, Infrared preheating to improve interlayer strength of big area additive manufacturing (BAAM) components,

Addit. Manuf. 14 (2017) 7–12. doi:10.1016/j.addma.2016.11.008.

[34] B.G. Compton, B.K. Post, C.E. Duty, L. Love, V. Kunc, Thermal analysis of additive manufacturing of large-scale thermoplastic polymer composites, Addit. Manuf. 17 (2017) 77–86. doi:10.1016/j.addma.2017.07.006.

[35] K. Choo, B. Friedrich, T. Daugherty, A. Schmidt, C. Patterson, M.A. Abraham, B. Conner, K. Rogers, P. Cortes, E. MacDonald, Heat retention modeling of large area additive manufacturing, Addit. Manuf. 28 (2019) 325–332. doi:10.1016/j.addma.2019.04.014.

[36] D. Moreno Nieto, V. Casal López, S.I. Molina, Large-format polymeric pellet-based additive manufacturing for the naval industry, Addit. Manuf. 23 (2018) 79–85. doi:10.1016/j.addma.2018.07.012.

[37] V. Kunc, J. Lindahl, R.B. Dinwiddie, B. Post, L. Love, C. Duty, M. Matlack, R.L. Fahey Jr, A.A. Hassen, Investigation of In-Autoclave Additive Manufacturing Composite Tooling, in: Compos. Adv. Mater. Expo Conf., 2016: pp. 1–9.

[38] C. Duty, C. Ajinjeru, V. Kishore, B. Compton, N. Hmeidat, X. Chen, P. Liu, A.A. Hassen, J. Lindahl, V. Kunc, What makes a material printable? A viscoelastic model for extrusion-based 3D printing of polymers, J. Manuf. Process. 35 (2018) 526–537. doi:10.1016/j.jmapro.2018.08.008.

[39] G. Grassi, S. Lupica Spagnolo, I. Paoletti, Fabrication and durability testing of a 3D printed façade for desert climates, Addit. Manuf. 28 (2019) 439–444. doi:10.1016/j.addma.2019.05.023.

[40] M. Pourali, A.M. Peterson, Thermal Modeling of Material Extrusion Additive Manufacturing, Polym. Addit. Manuf. Recent Dev. Part 7 - Therm. Model. Mater. Extrus. Addit. Manuf. (2019). doi:10.1021/bk-2019-1315.ch007.

[41] A. D'Amico, A.M. Peterson, An Adaptable FEA Simulation of Material Extrusion Additive Manufacturing Heat Transfer in 3D, Addit. Manuf. 21 (2018) 422–430. doi:10.1016/j.addma.2018.02.021.

[42] C.S. Davis, K.E. Hillgartner, S.H. Han, J.E. Seppala, Mechanical strength of welding zones produced by polymer extrusion additive manufacturing, Addit. Manuf. 16 (2017) 162–166.

doi:10.1016/j.addma.2017.06.006.

[43] J.E. Seppala, K.D. Migler, Infrared thermography of welding zones produced by polymer extrusion additive manufacturing, Addit. Manuf. 12 (2016) 71–76. doi:10.1016/j.addma.2016.06.007.

[44] MatWeb-Free-Cutting Brass, UNS C36000, O61 Temper 25 mm rod, (2017).

[45] UL Prospector ABS Data Sheet BT - UL Prospector, (2016).

[46] F. Szabó, J.G. Kovács, Development of a pressure-volume-temperature measurement method for thermoplastic materials based on compression injection molding, J. Appl. Polym. Sci. 131 (2014) 1–8. doi:10.1002/app.41140.

[47] N.A. Nguyen, C.C. Bowland, A.K. Naskar, Mechanical, thermal, morphological, and rheological characteristics of high performance 3D-printing lignin-based composites for additive manufacturing applications, Data Br. 19 (2018) 936–950. doi:10.1016/j.dib.2018.05.130.

[48] M.L. Williams, R.F. Landel, J.D. Ferry, The Temperature Dependence of Relaxation Mechanisms in Amorphous Polymers and Other Glass-forming Liquids, J. Am. Chem. Soc. 77 (1955) 3701–3707.

[49] T.J. Coogan, D.O. Kazmer, Healing simulation for bond strength prediction of FDM, Rapid Prototyp. J. 23 (2017) 551–561. doi:10.1108/RPJ-03-2016-0051.

[50] H.L. Tekinalp, V. Kunc, G.M. Velez-Garcia, C.E. Duty, L.J. Love, A.K. Naskar, C.A. Blue, S. Ozcan, Highly oriented carbon fiber–polymer composites via additive manufacturing, Compos. Sci. Technol. 105 (2014) 144–150. doi:10.1016/j.compscitech.2014.10.009.

[51] Y.H. Kim, R.P. Wool, A Theory of Healing at a Polymer-Polymer Interface, Macromolecules. 16 (1983) 1115–1120. doi:10.1021/ma00241a013.

[52] S. Prager, M. Tirrell, The healing process at polymer-polymer interfaces, J. Chem. Phys. 75 (1981) 5194–5198. doi:10.1063/1.441871.

[53] P.-G. DeGennes, Interpenetration of polymers at an interface, C. R. Seances Acad. Sci, Ser. B. 291 (1980) 219–221.

[54] R.P. Wool, K.M. O'Connor, A theory of crack healing in polymers, J. Appl. Phys. 52 (1981) 5953–5963.

[55] A. Roschli, K.T. Gaul, A.M. Boulger, B.K. Post, P.C. Chesser, L.J. Love, F. Blue, M. Borish, Designing for Big Area Additive Manufacturing, Addit. Manuf. 25 (2019) 275–285. doi:10.1016/j.addma.2018.11.006.

[56] Y. Aoki, A. Hatano, T. Tanaka, H. Watanabe, Nonlinear stress relaxation of ABS polymers in the molten state, Macromolecules. 34 (2001) 3100–3107. doi:10.1021/ma002076l.

[57] S.S. Babu, L. Love, R. Dehoff, W. Peter, T.R. Watkins, S. Pannala, Additive manufacturing of materials : Opportunities and challenges, MRS Bull. 40 (2015) 1154–1161. doi:10.1557/mrs.2015.234.